

¹ Weighted structure tensor total variation for image denoising

² **Xiuhan Sheng^a, Lijuan Yang^a, and Jingya Chang^{a,*}**

³ ^aGuangdong University of Technology, School of mathematics and statistics, 161 Yinglong Road, Tianhe District,

⁴ Guangzhou, China, 510520

⁵ **Abstract.** For image denoising problems, the structure tensor total variation (STV)-based models show good performances when compared with other competing regularization approaches. However, the STV regularizer does not couple the local information of the image and may not maintain the image details. Therefore, we employ the anisotropic weighted matrix introduced in the anisotropic total variation (ATV) model to improve the STV model. By applying the weighted matrix to the discrete gradient of the patch-based Jacobian operator in STV, our proposed weighted STV (WSTV) model can effectively capture local information from images and maintain their details during the denoising process. The optimization problem in the model is solved by a fast first-order gradient projection algorithm with a complexity result of $O(1/i^2)$. For images with different Gaussian noise levels, the experimental results demonstrate that the WSTV model can effectively improve the quality of restored images compared to other TV and STV-based models.

¹⁵ **Keywords:** image denoising, anisotropic total variation, structure tensor total variation, weighted matrix.

¹⁶ *Address all correspondence to Jingya Chang, jychang@gdut.edu.cn

¹⁷ 1 Introduction

¹⁸ As an important area in digital image processing,¹ image restoration covers topics of image denoising,^{2–4} deblurring,^{5–7} medical imaging,^{8–10} super-resolution reconstruction,^{11–13} and so on. During

²⁰ the processes of acquisition and transmission, noise signals inevitably contaminate digital images.

²¹ The purpose of image restoration is to restore clear images from degraded images and simultaneously preserve image details, such as textures and edges. In this paper, we mainly focus on image

²³ denoising.

²⁴ The variational method is one of the most widely used strategies for image denoising problems.

²⁵ For models in the variational method, a key point is the regularization term. Among the existing

²⁶ regularization terms, total variation (TV)¹⁴ is the most common one. TV can maintain sharp edges

²⁷ during noise removal, which overcomes the disadvantage of excessively smooth edges caused by

²⁸ Tikhonov regularization.¹⁵ The central disadvantage of TV is that it may bring artifact boundaries

29 in smooth regions.¹⁶ Numerous models are proposed to deal with such kinds of staircase effects;
30 for instance, the high-order total variation (HOTV),^{17,18} the total generalized variation (TGV),^{19,20}
31 and the nolocal total variation (NLTv).²¹ Compared to TV, these modified models exhibit better
32 restoration results and reduce staircase effects in some regions of the image.

33 In addition, Leflammatis et al. proposed the structure tensor total variation (STV) regulariza-
34 tion family,²² which is a modified version of TV as well. The difference between the STV model
35 and the abovementioned TV-based models is that STV proposes to penalize the ℓ_p norms of the
36 square root of the eigenvalues of the structure tensor rather than the gradient magnitude. The STV
37 model provides a more robust and richer measure of image variation than the TV-based methods do
38 by exploiting additional information from the neighborhood of every point. However, the isotropic
39 STV model treats the discrete gradients in the horizontal and vertical directions equally, which
40 ignores the variation in local features of the image. Ref. 23 proposes that the directional weighted
41 matrix in the directional total variation (DTV)²⁴ model can be combined with the STV model. The
42 improved model is particularly sensitive to unidirectional images and can effectively remove noise,
43 which is called the direction-guided structure tensor total variation (DSTV)²³ model. But the ap-
44 plication scenarios of this model are not very broad, which prompts us to find a proper way to
45 distinguish the gradients in different directions in the STV model and fully explore the underlying
46 image structures.

47 The STV model utilizes the discrete gradient of the image in the process of calculating the
48 image structure tensor. Therefore, inspired by the weighted matrix in the ATV model given by
49 Pang et al.,²⁵ we also consider using the anisotropic matrix to apply different weights to the dis-
50 crete gradient operator in the x -axis and y -axis directions in the STV model. As a result, the STV
51 model weighted by an anisotropic diffusion matrix, called weighted structure tensor total variation

52 (WSTV) is given, which penalizes the weighted gradient magnitude before penalizing the eigen-
53 values of the structure tensor. This allows the image gradients in each channel in STV to diffuse
54 along the tangent direction of local features, thereby effectively capturing the local information of
55 the image.

56 *1.1 Contributions*

57 In this work, we give a weighted structure tensor total variation model for the image denoising
58 problem. The main contributions of this paper are

- 59 • The WSTV regularization term is proposed for the image denoising minimization model.
60 Compared to the STV model, a weighted matrix is introduced to achieve varying degrees of
61 punishment for discrete gradients in the x and y directions. The WSTV model couples the
62 local features of the image and maintains its details well.
- 63 • The WSTV optimization model is solved by an effective first-order algorithm. We show the
64 equivalence of the original model and its dual problem. Also, we give an upper bound of
65 the Lipschitz constant of the dual problem so that the classical FISTA can be applied to the
66 dual problem efficiently. Theoretically, we prove the properties of the dual problem, which
67 guarantee the $O(1/i^2)$ convergence rate of the algorithm.
- 68 • Numerical experiments demonstrate that the proposed WSTV method is superior when com-
69 pared to a class of TV-based methods. For most of the grayscale and colored image denoising
70 problems in Section 4, the values of PSNR and SSIM produced by WSTV are the best.

71 The remainder of this paper is organized as follows. Some elementary knowledge related to
72 image denoising and several denoising models are briefly introduced in Sec. 2. In Sec. 3, the

73 WSTV model is given. In addition, we show the computation method that applies the fast gradient
 74 projection algorithm to the dual problem of the WSTV optimization model. In Sec. 4, we display
 75 and discuss the results of numerical experiments on images with different Gaussian noises. Finally,
 76 we conclude the paper in Sec. 5.

77 **2 Preliminaries**

78 In this section, we introduce the symbols and concepts used thereafter. The general linear image
 79 restoration models as well as TV and STV-based denoising models are reviewed.

80 *2.1 Notations*

Unless otherwise specified, vectors and matrices are represented by using lowercase and uppercase
 bold letters, respectively. We consider the vector-valued image $\mathbf{u} = (\mathbf{u}_1, \mathbf{u}_2, \dots, \mathbf{u}_M)$ of M
 channels for convenience, using N to represent the total number of pixels in each channel and
 stacking the channels to obtain $\mathbf{u} \in \mathbb{R}^{NM}$. Define $\Upsilon \in \mathcal{Y} \triangleq \mathbb{R}^{M \times N \times 2}$, then the $\ell_{2,1}$ norm of Υ is

$$\|\Upsilon\|_{2,1} = \sum_{i=1}^M \sum_{j=1}^N \sqrt{\sum_{s=1}^2 \Upsilon_{i,j,s}^2}$$

Apart from this $\ell_{2,1}$ norm, for $\Lambda = [\Lambda_1^T, \dots, \Lambda_M^T]^T \in \mathcal{Y}$, the norm $\|\Lambda\|_{q,p}$ for any $q \neq 2$ or $p \neq 1$
 represents

$$\|\Lambda\|_{q,p} = \left(\sum_{i=1}^M \|\Lambda_i\|_{\mathcal{S}_p}^q \right)^{1/q},$$

81 where $\|\cdot\|_{\mathcal{S}_p}$ represents the p -order Schatten norm. The norm $\|\cdot\|_{q,p}$ is also denoted as $\ell_q\mathcal{S}_p$.²²

Let $\Upsilon, \Lambda \in \mathcal{X} \triangleq \mathbb{R}^{N \times LM \times 2}$, with $\Upsilon_n, \Lambda_n \in \mathbb{R}^{LM \times 2}$ ($\forall n = 1, 2, \dots, N$). Then the inner

product $\langle \cdot, \cdot \rangle_{\mathcal{X}}$ and norm $\|\cdot\|_{\mathcal{X}}$ can be denoted by

$$\langle \Lambda, \Upsilon \rangle_{\mathcal{X}} = \sum_{n=1}^N \text{trace}(\Upsilon_n^T \Lambda_n)$$

and

$$\|\Upsilon\|_{\mathcal{X}} = \sqrt{\langle \Upsilon, \Upsilon \rangle_{\mathcal{X}}} = \left(\sum_{n=1}^N \|\Upsilon_n\|_F^2 \right)^{\frac{1}{2}},$$

where $\text{trace}(\cdot)$ is the trace operator of a matrix and $\|\cdot\|_F$ is the Frobenius norm. The symbol $B_{\infty,q}$ denotes ℓ_∞ - \mathcal{S}_q unit-norm ball, which is defined as

$$B_{\infty,q} = \{ \Phi \in \mathcal{X} : \|\Phi(n)\|_{\mathcal{S}_q} \leq 1, \forall n = 1, \dots, N \},$$

82 where $\Phi(n)$ represents the n -th submatrix of Φ .

83 *2.2 Image restoration model*

84 To address the ill-posed problem of image denoising, a basic linear image restoration model is
85 given as

$$\mathbf{f}(x) = \mathbf{A}\mathbf{u}(x) + \mathbf{n}(x), \quad (1)$$

86 where $\mathbf{u}(x) = (\mathbf{u}_1(x), \mathbf{u}_2(x), \dots, \mathbf{u}_M(x)) : \Omega \rightarrow \mathbb{R}^M$ is the expected restored image, and $\mathbf{f}(x) :$
87 $\Omega \rightarrow \mathbb{R}^M$ denotes the degraded image. Here \mathbf{A} is some linear bounded irreversible operator
88 mapping from one function space to another. For example, the linear operator \mathbf{A} is the identity
89 operator for image denoising. The $\mathbf{n}(x)$ denotes additional Gaussian noise, and $\Omega \subset \mathbb{R}^2$ denotes
90 the 2-dimensional image domain. The dimension M represents the number of image channels. In
91 order to recover the unknown image \mathbf{u} from Eq. (1), a general model for such an inverse problem

92 takes the following form

$$\min_{\mathbf{u}} \frac{1}{2} \|\mathbf{A}\mathbf{u} - \mathbf{f}\|_2^2 + \tau R(\mathbf{u}). \quad (2)$$

93 The former term of the model is the data fidelity term used to maintain the image structures, while
94 the latter is a regularization term. The regularization parameter $\tau \geq 0$ is used to balance both of
95 the above.

96 Generally, the total variation of noisy images is larger than that of non-noisy images. Therefore,
97 minimizing the total variation can eliminate noise. Image denoising based on total variation can
98 be summarized as the following minimization problem

$$\min_{\mathbf{u}} \frac{\tau}{2} \|\mathbf{u} - \mathbf{f}\|_2^2 + \|\nabla \mathbf{u}\|_{2,1}, \quad (3)$$

99 where $\nabla \mathbf{u}$ represents the discrete gradient obtained through the forward difference operator.²⁶ The
100 $\ell_{2,1}$ norm of $\nabla \mathbf{u}$ can be calculated by $\|\nabla \mathbf{u}\|_{2,1} = \sum_{i=1}^{NM} \sqrt{\sum_{s=1}^2 \nabla \mathbf{u}_{i,s}^2}$ since \mathbf{u} has been defined
101 as a vector.

102 2.3 Anisotropic total variation (ATV)

103 Actually, most TV-based models that we investigate are isotropic. The same weight is given when
104 we calculate the discrete gradient of the model, which results in the same penalty applied to both
105 the horizontal and vertical directions. However, this setting cannot well address the local features
106 in the process of restoring images. Consequently, Pang et al. proposed a new anisotropic total
107 variation (ATV).²⁵ In order to keep consistent with the formulae in Ref. 25, we define the grayscale
108 image $\mathbf{u} \in \mathbb{R}^{M \times N}$, i.e., \mathbf{u} is a matrix here. We clarify that the symbol \mathbf{u} refers to the vector-valued
109 image beyond this subsection. The ATV model can diffuse along the tangent direction of local

₁₁₀ features in the image by using an anisotropic weighted matrix, which assigns different weights to
₁₁₁ discrete gradients in the x and y directions. Specifically, it can be constructed by

$$\min_{\mathbf{u}} \frac{\tau}{2} \|\mathbf{u} - \mathbf{f}\|_2^2 + \|\mathcal{W} \nabla \mathbf{u}\|_{2,1}, \quad (4)$$

₁₁₂ where $\nabla \mathbf{u} \in \mathcal{Y}$. The anisotropic weighted matrix \mathcal{W} is defined as

$$\mathcal{W} = \begin{bmatrix} \mathbf{w}_1 & 0 \\ 0 & \mathbf{w}_2 \end{bmatrix} = \begin{bmatrix} \frac{1}{1+\kappa|\mathbf{G}_{\hat{\sigma}} * \nabla_x \mathbf{f}|} & 0 \\ 0 & \frac{1}{1+\kappa|\mathbf{G}_{\hat{\sigma}} * \nabla_y \mathbf{f}|} \end{bmatrix}, \quad (5)$$

₁₁₃ where κ and $\hat{\sigma}$ are parameters. The symbol $\mathbf{G}_{\hat{\sigma}}$ represents the Gaussian convolution of variance $\hat{\sigma}$
₁₁₄ to reduce the influence of noise. The model degenerates into TV when the operators \mathbf{w}_1 and \mathbf{w}_2
₁₁₅ take the same constant. Since the model (4) is a non-smooth convex optimization problem, the
₁₁₆ alternating direction method of multipliers (ADMM) can be used to solve it.

₁₁₇ 2.4 Structure tensor total variation (STV)

₁₁₈ The two TV-based models mentioned above penalize the gradient magnitude, which is completely
₁₁₉ localized. To address this limitation, Lefkimatis et al. proposed structure tensor total variation
₁₂₀ (STV),²² where the information available in the local neighborhood of each point in the image
₁₂₁ domain is taken into account. Then the structure tensor square root of the eigenvalues of the image
₁₂₂ is penalized. Therefore, the obtained regularizer exhibits semi-local behavior.

₁₂₃ Any pixel i of a vector-valued image \mathbf{u} has a Jacobian matrix, which is defined as

$$(\mathbf{J}\mathbf{u})(i) = [\nabla \mathbf{u}_1(i), \nabla \mathbf{u}_2(i), \dots, \nabla \mathbf{u}_M(i)]^T, \quad (6)$$

¹²⁴ where $\nabla \mathbf{u}_1(i)$ represents discrete gradient.²⁶ Define the structure tensor of image \mathbf{u} at pixel i as

$$(S_K \mathbf{u})(i) = K * [(\mathbf{J} \mathbf{u})(i)^T (\mathbf{J} \mathbf{u})(i)], \quad (7)$$

¹²⁵ where K is a Gaussian convolution kernel, and $*$ represents the convolution operation. Define
¹²⁶ $\lambda^+ = \lambda^+(S_K \mathbf{u}(i))$ and $\lambda^- = \lambda^-(S_K \mathbf{u}(i))$ as the maximum and minimum eigenvalues of the
¹²⁷ structure tensor $S_K \mathbf{u}(i)$ at any point i in image \mathbf{u} . From Ref. 22, we know that the ℓ_p norms of the
¹²⁸ square root of the eigenvalues of the structure tensor are more effective in measuring local image
¹²⁹ variation. Naturally, the STV regularizer can be defined as

$$\text{STV}_p(\mathbf{u}) = \sum_{i=1}^N \|(\sqrt{\lambda_i^+}, \sqrt{\lambda_i^-})\|_p, p \geq 1. \quad (8)$$

¹³⁰ Because of the nonlinearity of the operator and the existence of the convolution kernel K in
¹³¹ $S_K \mathbf{u}(i)$, Lefkimiatis et al.²² proposed an alternative formulation of $S_K \mathbf{u}(i)$ and named it patch-
¹³² based Jacobian $\mathbf{J}_K : \mathbb{R}^{NM} \rightarrow \mathbb{R}^{N \times LM \times 2}$. For any pixel i in the image \mathbf{u} , we have

$$(\mathbf{J}_K \mathbf{u})(i) = [\tilde{\nabla} \mathbf{u}_1(i), \tilde{\nabla} \mathbf{u}_2(i), \dots, \tilde{\nabla} \mathbf{u}_M(i)]^T, \quad (9)$$

¹³³ where $\tilde{\nabla} \mathbf{u}_1(i) = [(\Psi_1 \nabla \mathbf{u}_1)(i), (\Psi_2 \nabla \mathbf{u}_1)(i), \dots, (\Psi_L \nabla \mathbf{u}_1)(i)]$. In addition, $L = (2L_K + 1)^2$
¹³⁴ indicates the number of all elements in the convolution kernel K . The weighted translation
¹³⁵ operator $\Psi_l (l = 1, \dots, L)$ is defined as $(\Psi_l \nabla \mathbf{u}_m)(i) = \sqrt{K[g_l]} (\nabla \mathbf{u}_m)(x_i - g_l)$, where $g_l \in$
¹³⁶ $\{-L_K, \dots, L_K\}^2$ is the shift amount. Based on the above definition, the discrete structure tensor

¹³⁷ of \mathbf{u} evaluated at the pixel location i in terms of the patch-based Jacobian can be written as

$$(S_K \mathbf{u})(i) = ((\mathbf{J}_K \mathbf{u})(i))^T (\mathbf{J}_K \mathbf{u})(i). \quad (10)$$

¹³⁸ Lefkimiatis et al.²² have also proved that the singular values of $(\mathbf{J}_K \mathbf{u})(i)$ are equivalent to the

¹³⁹ square root of the eigenvalues of $(S_K \mathbf{u})(i)$. Then the STV regularizer in Eq. (8) can be redefined

¹⁴⁰ as

$$\text{STV}_p(\mathbf{u}) = \sum_{i=1}^N \|(\mathbf{J}_K \mathbf{u})(i)\|_{\mathcal{S}_p} = \|\mathbf{J}_K \mathbf{u}\|_{1,p}. \quad (11)$$

¹⁴¹ 3 The proposed model and algorithm

¹⁴² 3.1 The weighted structure tensor total variation (WSTV) model

¹⁴³ In order to fully explore the local features of the image, we employ the anisotropic weighted matrix

¹⁴⁴ proposed in the ATV model to refine the patch-based Jacobian operator of the STV model. The

¹⁴⁵ new weighted patch-based Jacobian $(\widehat{\mathbf{J}}_K \mathbf{u})(i)$ can be represented as

$$(\widehat{\mathbf{J}}_K \mathbf{u})(i) = [\widehat{\nabla} \mathbf{u}_1(i), \widehat{\nabla} \mathbf{u}_2(i), \dots, \widehat{\nabla} \mathbf{u}_M(i)]^T, \quad (12)$$

¹⁴⁶ where $\widehat{\nabla} \mathbf{u}_1(i) = [(\Psi_1 \mathcal{W} \nabla \mathbf{u}_1)(i), (\Psi_2 \mathcal{W} \nabla \mathbf{u}_1)(i), \dots, (\Psi_L \mathcal{W} \nabla \mathbf{u}_1)(i)]$. Here \mathcal{W} represents the

¹⁴⁷ anisotropic weighted matrix defined in Eq. (5). Furthermore, the existence of \mathcal{W} will not destroy

¹⁴⁸ the convexity of the regularizer. The WSTV regularizer can be defined as

$$\text{WSTV}_p(\mathbf{u}) = \sum_{i=1}^N \|(\widehat{\mathbf{J}}_K \mathbf{u})(i)\|_{\mathcal{S}_p} = \|\widehat{\mathbf{J}}_K \mathbf{u}\|_{1,p}. \quad (13)$$

¹⁴⁹ According to the objective function given in Eq. (2), the problem to be solved is

$$\min_{\mathbf{u} \in \mathcal{C}} \frac{1}{2} \|\mathbf{u} - \mathbf{f}\|_2^2 + \tau \|\widehat{\mathbf{J}}_K \mathbf{u}\|_{1,p}. \quad (14)$$

¹⁵⁰ Since the WSTV regularizer is convex, the minimizer $\hat{\mathbf{u}}$ is the proximal point generated by the
¹⁵¹ proximal operator associated with the regularizer WSTV_p at \mathbf{f} , i.e.,

$$\hat{\mathbf{u}} = \text{prox}_{\tau \text{WSTV}_p(\mathbf{u})}(\mathbf{f}) := \arg \min_{\mathbf{u} \in \mathcal{C}} \frac{1}{2} \|\mathbf{u} - \mathbf{f}\|_2^2 + \tau \|\widehat{\mathbf{J}}_K \mathbf{u}\|_{1,p}, \quad (15)$$

¹⁵² where \mathcal{C} is a convex set that represents additional constraints on the solution. In this paper, we
¹⁵³ consider the box constraints ($\mathcal{C} = \mathbb{R}^{NM}$ in unconstrained case).

¹⁵⁴ 3.2 Algorithm for WSTV

¹⁵⁵ Since the suggested WSTV regularizer is not differentiable, we consider a dual formulation for
¹⁵⁶ the optimization problem (15). We show the computation framework in two steps. First, the
¹⁵⁷ dual model as well as the equivalence between the primal and dual problems are deduced. The
¹⁵⁸ convexity, Lipschitz continuity, and solvability of the dual model are also proved. Then, we employ
¹⁵⁹ the fast gradient projection method to find the optimal solution of the dual model. Moreover, details
¹⁶⁰ and the complexity result $O(1/i^2)$ of the algorithm are given.

¹⁶¹ **Lemma 1.** Let $p \geq 1$, and let q be the conjugate exponent of p , i.e., $\frac{1}{p} + \frac{1}{q} = 1$. Then, the mixed vector-matrix norm

¹⁶² $\|\cdot\|_{\infty,q}$ is dual to the mixed vector-matrix norm $\|\cdot\|_{1,p}$ ²⁷.

¹⁶³ Through Lemma 1 and the property that the dual of the dual norm is the original norm, we are

¹⁶⁴ able to redefine the WSTV regularizer in terms of

$$\|\widehat{\mathbf{J}}_K \mathbf{u}\|_{1,p} = \max_{\Phi \in B_{\infty,q}} \langle \Phi, \widehat{\mathbf{J}}_K \mathbf{u} \rangle_{\mathcal{X}}, \quad (16)$$

¹⁶⁵ where Φ denotes the variable in the target space $\mathcal{X} \triangleq \mathbb{R}^{N \times LM \times 2}$. Then, we can rewrite Eq. (15) as

¹⁶⁶ follows

$$\begin{aligned} \hat{\mathbf{u}} &= \arg \min_{\mathbf{u} \in \mathcal{C}} \frac{1}{2} \|\mathbf{u} - \mathbf{f}\|_2^2 + \tau \max_{\Phi \in B_{\infty,q}} \langle \Phi, \widehat{\mathbf{J}}_K \mathbf{u} \rangle_{\mathcal{X}} \\ &= \arg \min_{\mathbf{u} \in \mathcal{C}} \frac{1}{2} \|\mathbf{u} - \mathbf{f}\|_2^2 + \tau \max_{\Phi \in B_{\infty,q}} \langle \widehat{\mathbf{J}}_K^* \Phi, \mathbf{u} \rangle_2. \end{aligned} \quad (17)$$

¹⁶⁷ The adjoint operator $\widehat{\mathbf{J}}_K^* : \mathbb{R}^{N \times LM \times 2} \rightarrow \mathbb{R}^{NM}$ of the weighted patch-based Jacobian $\widehat{\mathbf{J}}_K$ is
¹⁶⁸ defined as

$$(\widehat{\mathbf{J}}_K^* \mathbf{X})(t) = \sum_{l=1}^L -\text{div}_{(\delta)}(\Psi_l^* \mathbf{X}(i, h)), \quad (18)$$

¹⁶⁹ where $h = (m-1)L + l$ and $t = (m-1)N + n$ with $1 \leq n \leq N$ and $1 \leq m \leq M$. The symbol
¹⁷⁰ Ψ_l^* is the adjoint of the weighted translation operator Ψ_l , which scans the $\mathbf{X}(i, h)$ in column-
¹⁷¹ wise manner. The two-element vector $\mathbf{X}(i, h)$ is the h th row of the i th submatrix of an arbitrary
¹⁷² $\mathbf{X} \in \mathbb{R}^{N \times LM \times 2}$ [22, Proposition 3.2]. The weighted discrete divergence operator $\text{div}_{(\delta)}$ is denoted
¹⁷³ by

$$\text{div}_{(\delta)}(\cdot) \triangleq \text{div}(\mathcal{W}^T(\cdot)) = \text{div}(\mathcal{W}(\cdot)). \quad (19)$$

¹⁷⁴ Here div represents the discrete divergence, which is defined using backward differences.²⁶

¹⁷⁵ The Eq. (17) is rewritten as a minimax problem

$$\min_{\mathbf{u} \in \mathcal{C}} \max_{\Phi \in B_{\infty,q}} H(\mathbf{u}, \Phi), \quad (20)$$

176 where $H(\mathbf{u}, \Phi) = \frac{1}{2}\|\mathbf{u} - \mathbf{f}\|_2^2 + \tau\langle \widehat{\mathbf{J}}_K^* \Phi, \mathbf{u} \rangle_2$. Since the function $H(\mathbf{u}, \Phi)$ is convex with respect
 177 to \mathbf{u} and concave with respect to Φ , there is a common saddle point $(\hat{\mathbf{u}}, \hat{\Phi})$ that does not change
 178 when the minimum and the maximum are interchanged. Specifically, we have

$$\min_{\mathbf{u} \in \mathcal{C}} \max_{\Phi \in B_{\infty,q}} H(\mathbf{u}, \Phi) = H(\hat{\mathbf{u}}, \hat{\Phi}) = \max_{\Phi \in B_{\infty,q}} \min_{\mathbf{u} \in \mathcal{C}} H(\mathbf{u}, \Phi). \quad (21)$$

179 Maximizing the dual objective function $d(\Phi) = \min_{\mathbf{u} \in \mathcal{C}} H(\mathbf{u}, \Phi)$ in Eq. (21) is equivalent to minimiz-
 180 ing the primal objective function $p(\mathbf{u}) = \max_{\Phi \in B_{\infty,q}} H(\mathbf{u}, \Phi)$. As a result, we can find the minimizer
 181 $\hat{\mathbf{u}}$ of $p(\mathbf{u})$ by seeking the maximizer $\hat{\Phi}$ of $d(\Phi)$. The minimization problem of \mathbf{u} can be obtained
 182 by expanding the function $H(\mathbf{u}, \Phi)$, i.e.,

$$\hat{\mathbf{u}} = \operatorname{argmin}_{\mathbf{u} \in \mathcal{C}} \|\mathbf{u} - (\mathbf{f} - \tau \widehat{\mathbf{J}}_K^* \Phi)\|_2^2 - D, \quad (22)$$

183 where D represents a constant term and the solution of Eq. (22) is $\hat{\mathbf{u}} = P_{\mathcal{C}}(\mathbf{f} - \tau \widehat{\mathbf{J}}_K^* \Phi)$. The
 184 operator $P_{\mathcal{C}}$ is the orthogonal projection operator on the convex set \mathcal{C} . By substituting $\hat{\mathbf{u}}$ into the
 185 function $H(\mathbf{u}, \Phi)$, we have

$$d(\Phi) = H(\hat{\mathbf{u}}, \Phi) = \frac{1}{2}\|\mathbf{s} - P_{\mathcal{C}}(\mathbf{s})\|_2^2 + \frac{1}{2}\|\mathbf{f}\|_2^2 - \frac{1}{2}\|\mathbf{s}\|_2^2, \quad (23)$$

186 where $\mathbf{s} = \mathbf{f} - \tau \widehat{\mathbf{J}}_K^* \Phi$. Therefore, the dual problem of the WSTV model is finally presented as

$$\hat{\Phi} = \arg \max_{\Phi \in B_{\infty,q}} d(\Phi) = \arg \max_{\Phi \in B_{\infty,q}} \frac{1}{2}\|\mathbf{s} - P_{\mathcal{C}}(\mathbf{s})\|_2^2 + \frac{1}{2}\|\mathbf{f}\|_2^2 - \frac{1}{2}\|\mathbf{s}\|_2^2. \quad (24)$$

187 In the next theorem, we show the properties of the dual problem.

188 **Theorem 1.** The dual optimization model in (24) satisfies the following properties

189 (1) The objective function $d(\Phi)$ is convex;

190 (2) The gradient of $d(\Phi)$ is Lipschitz continuous with Lipschitz constant $L(d) = 8\sqrt{2}\tau^2$;

191 (3) The dual optimization problem is solvable, i.e., $\hat{\Phi}$ is not an empty set.

192 **Proof.** (1) Because $H(\mathbf{u}, \Phi)$ is concave with respect to Φ , then $\sup_{\mathbf{u} \in \mathcal{C}} \{-H(\mathbf{u}, \Phi)\}$ is a convex

193 function with respect to Φ . That is to say, $d(\Phi) = \min_{\mathbf{u} \in \mathcal{C}} H(\mathbf{u}, \Phi)$ is a convex function. The first

194 part of the theorem holds.

195 (2) Similar to Proposition 4.2 in Ref. 22, we have

$$\begin{aligned} \|\nabla d(\mathbf{a}) - \nabla d(\mathbf{b})\| &= \tau \|\widehat{\mathbf{J}}_K P_C(\mathbf{f} - \tau \widehat{\mathbf{J}}_K^* \mathbf{a}) - \widehat{\mathbf{J}}_K P_C(\mathbf{f} - \tau \widehat{\mathbf{J}}_K^* \mathbf{b})\| \\ &\leq \tau \|\widehat{\mathbf{J}}_K\| \|P_C(\mathbf{f} - \tau \widehat{\mathbf{J}}_K^* \mathbf{a}) - P_C(\mathbf{f} - \tau \widehat{\mathbf{J}}_K^* \mathbf{b})\| \\ &\leq \tau \|\widehat{\mathbf{J}}_K\| \|\tau \widehat{\mathbf{J}}_K^* (\mathbf{a} - \mathbf{b})\| \\ &\leq \tau^2 \|\widehat{\mathbf{J}}_K\|^2 \|\mathbf{a} - \mathbf{b}\| \\ &\leq \tau^2 \|\mathcal{W}\|^2 \|\nabla\|^2 \|T\|^2 \|\mathbf{a} - \mathbf{b}\|, \end{aligned}$$

196 where $T = \sum_{l=1}^L (\Psi_l^* \Psi_l)$. It is proved in Ref. 29 that $\|\nabla\|^2 \leq 8$ and $\|T\|^2 \leq \sqrt{2}$, and further we

197 have $\|\mathcal{W}\|^2 \leq \max\{\mathbf{w}_1^2, \mathbf{w}_2^2\}^2 \leq 1$. These indicate that $L(d) = 8\sqrt{2}\tau^2$.

198 (3) Since the objective function $d(\Phi)$ is smooth and the constraint $\Phi \in B_{\infty, q}$ is compact, the
199 dual problem is solvable. The proof is completed.

200 Because the dual problem is smooth and convex, we are able to apply the fast gradient projec-
201 tion method (FGP)²⁹ to solve it. In each iteration, a transitional point is obtained by the gradient

202 projection method. Then, a new iteration point is generated by the accelerated technique in FISTA
 203 from the transitional point and the previous point. The detailed computational process involves
 204 the gradient of the objective function in (24), the step size of the first-order algorithm, and the
 205 projection onto the constraint $B_{\infty,q}$.

The gradient of the objective function in the dual problem is

$$\nabla d(\Phi) = \tau \widehat{\mathbf{J}}_K P_{\mathcal{C}}(\mathbf{f} - \tau \widehat{\mathbf{J}}_K^* \Phi).$$

206 For the step size along the gradient ascent direction, a constant of $1/L(d)$ is chosen to ensure
 207 the convergence of the FGP algorithm. Here, $L(d)$ represents the Lipschitz constant whose upper
 208 bound $\leq 8\sqrt{2}\tau^2$ is proved in Theorem 1. In terms of the projection of a matrix on the unit normal
 209 ball $B_{\infty,q}$, the authors of Ref. 22 proved that it can be calculated with the aid of the SVD decom-
 210 position of the matrix. Below we give the explicit steps for calculating the projection of $\Phi(n)$ on
 211 $B_{\infty,q}$.

212 (1) Conduct SVD to $\Phi(n)$, i.e., $\Phi(n) = \mathbf{U}\Sigma\mathbf{V}^T$, where $\Sigma = \text{diag}(\sigma_1, \sigma_2)$.

213 (2) Calculate the projection of $\Phi(n)$ onto the unit-norm ball B_{S_q} , i.e., $P_{B_{S_q}}(\Phi(n)) = \mathbf{U}\Sigma_q\mathbf{V}^T$,
 214 where $\Sigma_q = \text{diag}(\sigma_q)$ and σ_q are the projected singular values of Σ onto the ℓ_q unit-norm
 215 ball $B_q = \{\boldsymbol{\sigma} \in \mathbb{R}_+^N : \|\boldsymbol{\sigma}\|_q \leq 1\}$.

216 (3) Compute \mathbf{V} and Σ using the eigenvalue decomposition of $(\Phi(n))^T(\Phi(n))$.

217 (4) The projection can be constructed by $P_{B_{S_q}}(\Phi(n)) = \Phi(n)\mathbf{V}\Sigma^+\Sigma_q\mathbf{V}^T$. Σ^+ is the pseudoin-
 218 verse matrix of Σ .

219 We only consider the case of $q = \infty$ in this work. Therefore, we have

$$P_{B_{S_\infty}}(\Phi(n)) = \Phi(n) \mathbf{V} \Sigma^+ \text{diag}(\min(\sigma(\Phi(n)), \mathbf{1})) \mathbf{V}^T, \quad (25)$$

220 where $\mathbf{1}$ is a vector with all elements set to one and $\sigma(\Phi(n)) \in \mathbb{R}_+^2$. Discussions about $q = 1, 2$ and
221 other situations can be found in Refs. 27 and 31. Finally, we present the complete computational process in Algorithm 1.

Algorithm 1 : FGP algorithm for WSTV-based denoising.

Input: $f, \tau > 0, p = 1, P_C$.

1: Initialize: $\Phi_0 = \mathbf{0} \in \mathbb{R}^{N \times LM \times 2}, t_1 = 1, i = 1$.

2: **while** stopping criterion is not satisfied **do**

3: $z = P_C(f - \tau \widehat{\mathbf{J}}_K^* \Phi_{i-1})$

4: $\Phi_i = P_{B_{\infty, \infty}}(\Phi_{i-1} + \frac{1}{8\sqrt{2}\tau} \widehat{\mathbf{J}}_K z)$

5: $t_{i+1} = \frac{1+\sqrt{1+4t_i^2}}{2}$

6: $\Phi_{i+1} = \Phi_k + (\frac{t_i-1}{t_{i+1}})(\Phi_i - \Phi_{i-1})$

7: $i = i + 1$

8: **end while**

Output: $\hat{u} = P_C(f - \tau \widehat{\mathbf{J}}_K^* \Phi_i)$.

222

223 The above FGP method can be regarded as a special case of the FISTA approach for constrained
224 optimization problems. Thus, the properties of the dual problem proved in Theorem 1 guarantee
225 that [30, Theorem 4.4]

$$d(\Phi_i) - d(\Phi^*) \leq \frac{2L(d)\|\Phi_0 - \Phi^*\|^2}{(i+1)^2}, \quad (26)$$

226 where Φ^* represents the optimal point. Hence, the complexity result for Algorithm 1 is $O(1/i^2)$.

227 **4 Numerical experiment**

228 In this section, the experimental results are presented to assess the performance of the proposed
229 WSTV model. We mainly focus on the comparisons between the WSTV model and other TV-

230 based models, such as the TV, ATV, VTV, and STV models. All of the numerical experiments
 231 are carried out using MATLAB (R2019a) on a Windows 10 (64-bit) desktop computer powered
 232 by an Intel Core i7 CPU running at 2.70 GHz and 8.0GB of RAM. We employ the structural
 233 similarity index (SSIM) and peak signal-to-noise ratio (PSNR) to evaluate the recovered quality of
 234 each method. In addition, the intensity of the image involved in the experiment is normalized to
 235 the range $[0, 1]$. Furthermore, all numerical methods will be stopped when the relative difference
 236 between two successive iterations satisfies

$$\frac{\|u^{i+1} - u^i\|_2}{\|u^i\|_2} \leq 10^{-5}$$

237 or after reaching a maximum number of iterations. The maximum number of iterations for TV,
 238 ATV, and VTV is set to 500, while STV and WSTV have a maximum of 100. The test images in
 239 Figure 1 are public domain images of digital image processing.

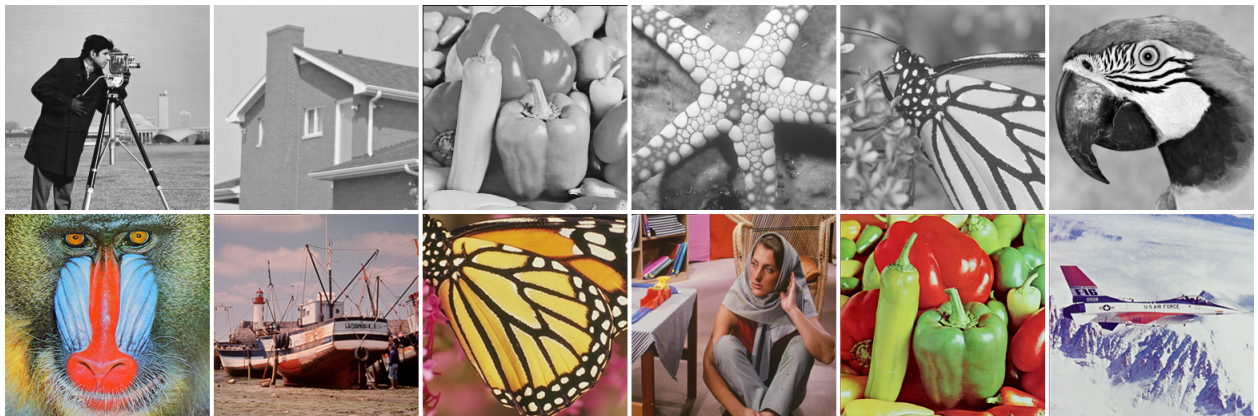


Fig 1 Twelve 256×256 test images. From left to right and top to bottom: Cameraman, House, Peppers, Starfish, Butterfly, Parrot, Baboon, Boats, Colored butterfly, Babara, Colored peppers and Airplane.

240 The regularization parameter τ , which controls how much filtering is introduced by the regu-
 241 larization term, has a significant impact on the effectiveness of the model restoration. We adjust
 242 the regularization parameters of the five models to empirically make the numerical performance of

243 each method achieve its best.

244 For the tested grayscale images, Cameraman, House, Peppers, Starfish, Butterfly, and Parrot.

245 Cameraman and House are mainly composed of smooth regions, while Butterfly and Parrot have

246 more edges and textures, respectively. We generate test data by introducing Gaussian noise with

247 standard deviations of $\sigma = \{0.01, 0.05, 0.1, 0.15\}$. Table 1 reveals that four models all exhibit

248 strong restoration performance at low noise levels $\sigma = \{0.01, 0.05\}$. As we add very little noise,

249 most details of the image can be preserved during the process of image restoration. Our model

250 produces higher PSNR and SSIM than those TV-based models at high Gaussian noise levels $\sigma =$

251 $\{0.1, 0.15\}$.

252 To effectively demonstrate the performance of the mentioned models for restoring images, we

253 enlarge a portion of the restored image, as shown in Figure 2. We observe that TV still retains a

254 large amount of noise in the smooth part of Cameraman, and the edges are relatively blurry. ATV

255 has obvious staircase effects but only retains a small amount of noise, while STV and our WSTV

256 model perform well.

257 In fact, our model is more effective at restoring details such as edges and corners compared

258 with STV. We display the differences between the restored image and the original image in Figure

259 3. It is worth noting that the darker the image color, the better the restoration effect. We note the

260 differences exist in Peppers, and there are still many areas with higher brightness in TV, such as

261 the upper right corner of the image. The brightness of the lower edge of ATV is obvious, which

262 indicates that ATV excessively magnifies the local features of the image. Obviously, our model

263 is the darkest, with neat image edges and sufficient details, which means that our method is more

264 robust than other models in restoring the degraded images.

265 For colored image denoising problems, the WSTV method is compared with the vector-extended

²⁶⁶ VTV³² of TV. Table 2 reports the PSNR and SSIM values obtained by three models under different
²⁶⁷ Gaussian noise levels. Similar to gray image denoising, all three models exhibit good restoration
²⁶⁸ performance at lower levels of Gaussian noise. In the images of Barbara and Peppers, STV and
²⁶⁹ WSTV generate the same SSIM, which we believe is caused by the addition of less noise. At high
²⁷⁰ noise levels, our model is significantly superior to the first two.

²⁷¹ A special case is Baboon, where STV produces better PSNR values than our model at noise
²⁷² levels of $\sigma = \{0.01, 0.05\}$. In fact, we observe that the details of Baboon are very abundant,
²⁷³ which means that the local information of the image is more complex. Weighting the discrete
²⁷⁴ gradient may have an impact on the information in the pixel domain of images and then reduce the
²⁷⁵ effectiveness of image restoration if the diagonal elements of the anisotropic diffusion matrix are
²⁷⁶ large. Moreover, we show the partial restored images of the three denoising models with Gaussian
²⁷⁷ noise levels of $\sigma = \{0.05, 0.1, 0.15\}$ in Figure 4. It explicitly demonstrates the superiority of our
²⁷⁸ model in color image denoising for preserving more details of the images.

Table 1 Compare the PSNR and SSIM of different models in grayscale image denoising.

Noise	0.01		0.05		0.10		0.15	
Image	Cameraman							
Models	PSNR	SSIM	PSNR	SSIM	PSNR	SSIM	PSNR	SSIM
TV	40.6641	0.9639	30.9808	0.8224	27.4314	0.7269	25.7675	0.7306
ATV	40.5000	0.9649	31.3241	0.8776	27.9608	0.8076	26.1333	0.7596
STV	41.8871	0.9762	31.4690	0.8893	28.0404	0.8077	26.1356	0.7557
WSTV	41.9646	0.9764	31.7752	0.8900	28.4345	0.8211	26.5238	0.7728
Image	Butterfly							
Models	PSNR	SSIM	PSNR	SSIM	PSNR	SSIM	PSNR	SSIM
TV	39.3814	0.9757	30.7683	0.8773	27.2040	0.8035	25.5354	0.7922
ATV	40.8081	0.9774	31.3426	0.9098	27.5779	0.8450	25.4152	0.7886
STV	41.8958	0.9845	31.7535	0.9285	27.9748	0.8617	25.8979	0.8113
WSTV	41.9860	0.9845	32.0720	0.9282	28.4314	0.8739	26.3218	0.8246
Image	Peppers							
Models	PSNR	SSIM	PSNR	SSIM	PSNR	SSIM	PSNR	SSIM
TV	25.5367	0.9366	24.6559	0.8172	23.7426	0.7391	23.2832	0.7377
ATV	40.6151	0.9706	31.8390	0.8838	28.2698	0.8142	26.1667	0.7562
STV	41.7389	0.9782	32.5765	0.9067	29.0054	0.8378	27.0236	0.7885
WSTV	41.7927	0.9783	32.7879	0.9064	29.4400	0.8510	27.4317	0.8026
Image	Parrot							
Models	PSNR	SSIM	PSNR	SSIM	PSNR	SSIM	PSNR	SSIM
TV	40.9081	0.9701	30.7923	0.8376	27.2613	0.7483	25.6409	0.7454
ATV	40.4617	0.9695	30.8887	0.8769	27.4686	0.8040	25.6610	0.7551
STV	41.7878	0.9811	31.3773	0.8951	27.9851	0.8196	26.0868	0.7698
WSTV	41.8670	0.9812	31.6405	0.8948	28.2974	0.8291	26.4374	0.7813
Image	House							
Models	PSNR	SSIM	PSNR	SSIM	PSNR	SSIM	PSNR	SSIM
TV	40.3755	0.9612	31.8646	0.8035	28.8632	0.7185	27.9519	0.7420
ATV	40.6282	0.9586	33.1480	0.8571	30.2274	0.8098	28.2457	0.7698
STV	42.1200	0.9723	33.7020	0.8726	30.5140	0.8100	28.6823	0.7701
WSTV	42.1399	0.9723	33.7861	0.8712	30.9519	0.8245	29.0902	0.7872
Image	Starfish							
Models	PSNR	SSIM	PSNR	SSIM	PSNR	SSIM	PSNR	SSIM
TV	39.3999	0.9775	30.2435	0.8689	26.7045	0.7742	24.9694	0.7245
ATV	40.2862	0.9792	30.3286	0.8820	26.5618	0.7833	24.4564	0.7024
STV	41.4311	0.9854	31.1023	0.9009	27.4800	0.8163	25.5208	0.7501
WSTV	41.4639	0.9854	31.2817	0.9024	27.6146	0.8211	25.6366	0.7558

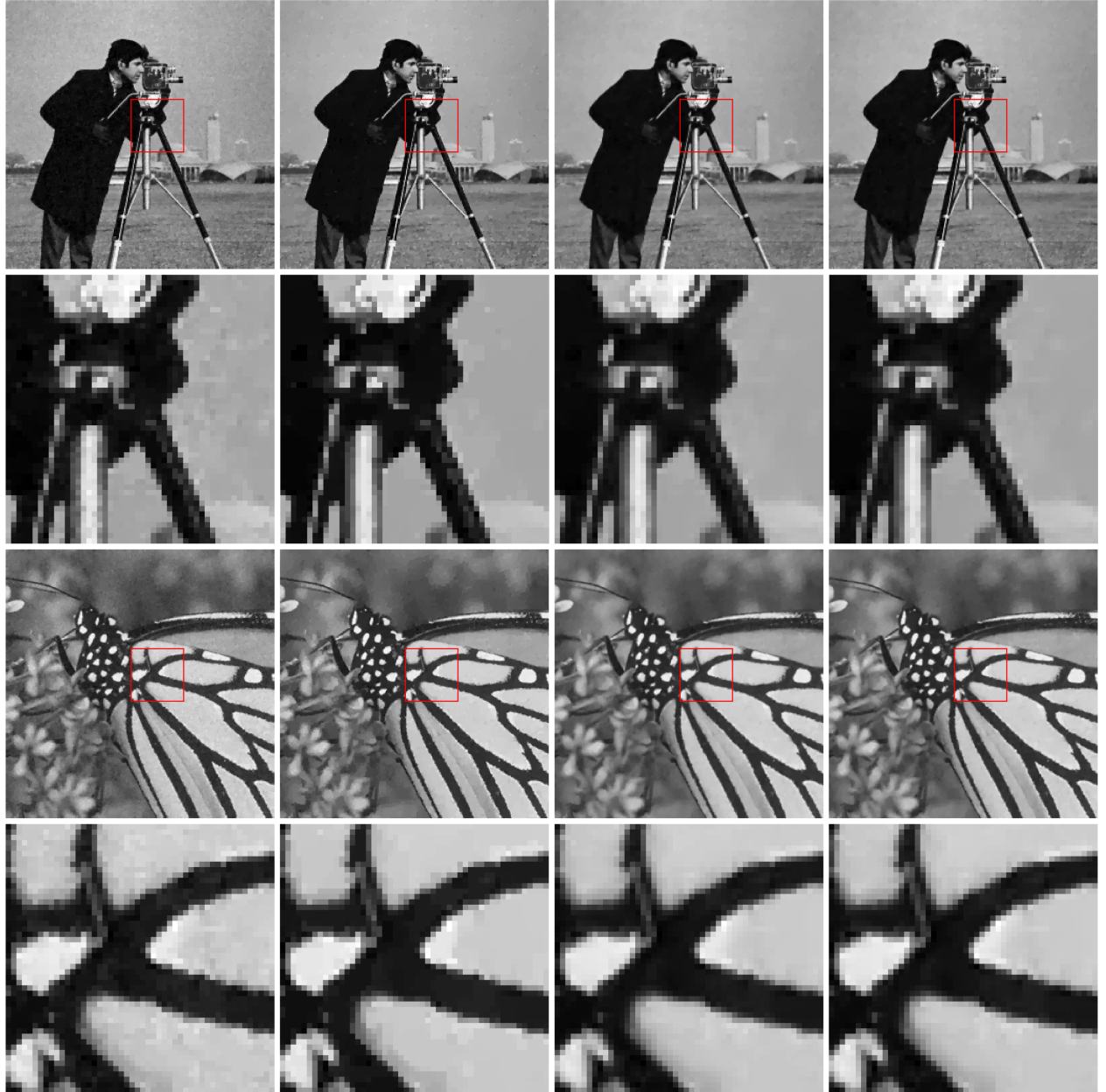


Fig 2 Compare the denoising effects of various models on grayscale images at the Gaussian noise level $\sigma = 0.05$. From left to right are the image restoration results obtained using TV, ATV, STV, and the proposed model (WSTV). The first row of each image represents the complete restored image. The second row of each image is a part of the restored image.

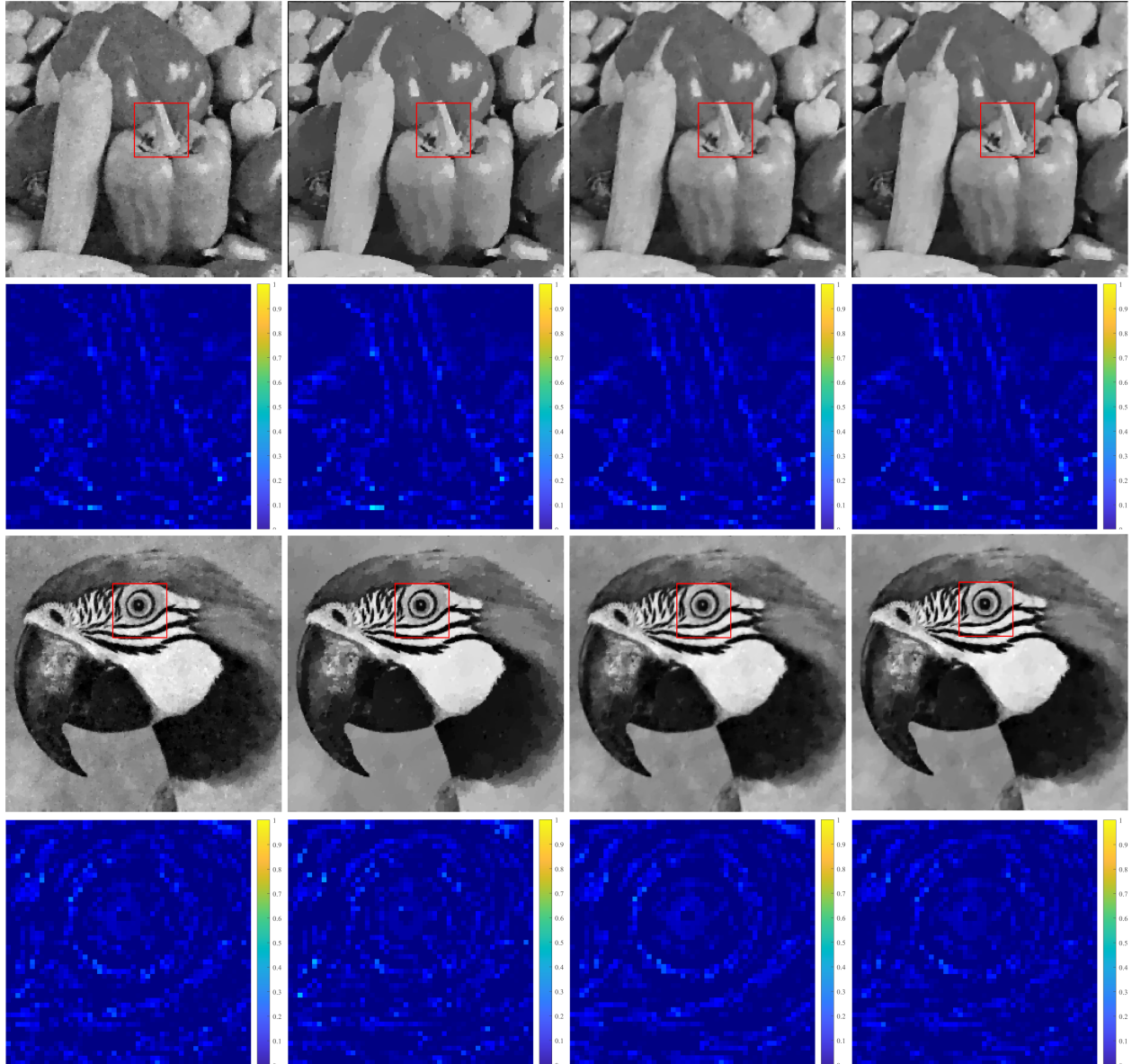


Fig 3 Compare the denoising effects of various models on grayscale images at the Gaussian noise level $\sigma = 0.1$. From left to right are the image restoration results obtained using TV, ATV, STV, and the proposed model (WSTV). The first row of each image represents the complete restored image. The second row of each image is the difference between the restored image and the original image. The colorbar displays more efficient restorations if the color is more shaded.

Table 2 Compare the PSNR and SSIM of different models in color image denoising.

Noise	0.01		0.05		0.10		0.15	
Image	Airplane							
Models	PSNR	SSIM	PSNR	SSIM	PSNR	SSIM	PSNR	SSIM
VTV	41.7862	0.9839	31.5210	0.9185	27.8202	0.8622	25.8642	0.8006
STV	41.8572	0.9828	31.7607	0.9159	27.9789	0.8406	26.0484	0.8053
WSTV	42.0402	0.9838	32.1803	0.9274	28.4510	0.8733	26.4042	0.8237
Image	Baboon							
Models	PSNR	SSIM	PSNR	SSIM	PSNR	SSIM	PSNR	SSIM
VTV	39.6139	0.9958	27.5152	0.9306	23.6604	0.8287	22.0993	0.7595
STV	39.9461	0.9961	27.8504	0.9358	24.1083	0.8481	22.2328	0.7638
WSTV	40.0153	0.9961	27.9325	0.9363	23.9745	0.8395	22.2351	0.7625
Image	Babara							
Models	PSNR	SSIM	PSNR	SSIM	PSNR	SSIM	PSNR	SSIM
VTV	40.8893	0.9931	30.3346	0.9399	26.7817	0.8877	25.0124	0.8460
STV	41.1515	0.9935	30.7391	0.9429	27.1864	0.8918	25.3847	0.8539
WSTV	41.2126	0.9935	30.8368	0.9435	27.3048	0.8955	25.4745	0.8568
Image	Boats							
Models	PSNR	SSIM	PSNR	SSIM	PSNR	SSIM	PSNR	SSIM
VTV	41.4372	0.9912	30.7406	0.9409	27.0070	0.8854	25.1392	0.8342
STV	41.6649	0.9909	31.1500	0.9428	27.3744	0.8830	25.4324	0.8440
WSTV	41.8123	0.9915	31.3970	0.9484	27.6057	0.8971	25.6314	0.8523
Image	Colored butterfly							
Models	PSNR	SSIM	PSNR	SSIM	PSNR	SSIM	PSNR	SSIM
VTV	41.5569	0.9981	31.0870	0.9831	27.2465	0.9628	25.0895	0.9413
STV	41.6655	0.9980	31.2932	0.9835	27.3596	0.9622	25.2968	0.9436
WSTV	41.8142	0.9981	31.6081	0.9848	27.7958	0.9663	25.6597	0.9474
Image	Colored peppers							
Models	PSNR	SSIM	PSNR	SSIM	PSNR	SSIM	PSNR	SSIM
VTV	41.4440	0.9984	31.8107	0.9869	28.3800	0.9728	26.4494	0.9587
STV	41.6158	0.9985	32.1747	0.9878	28.5737	0.9735	26.7581	0.9614
WSTV	41.7445	0.9985	32.5572	0.9888	29.1003	0.9765	27.1139	0.9641

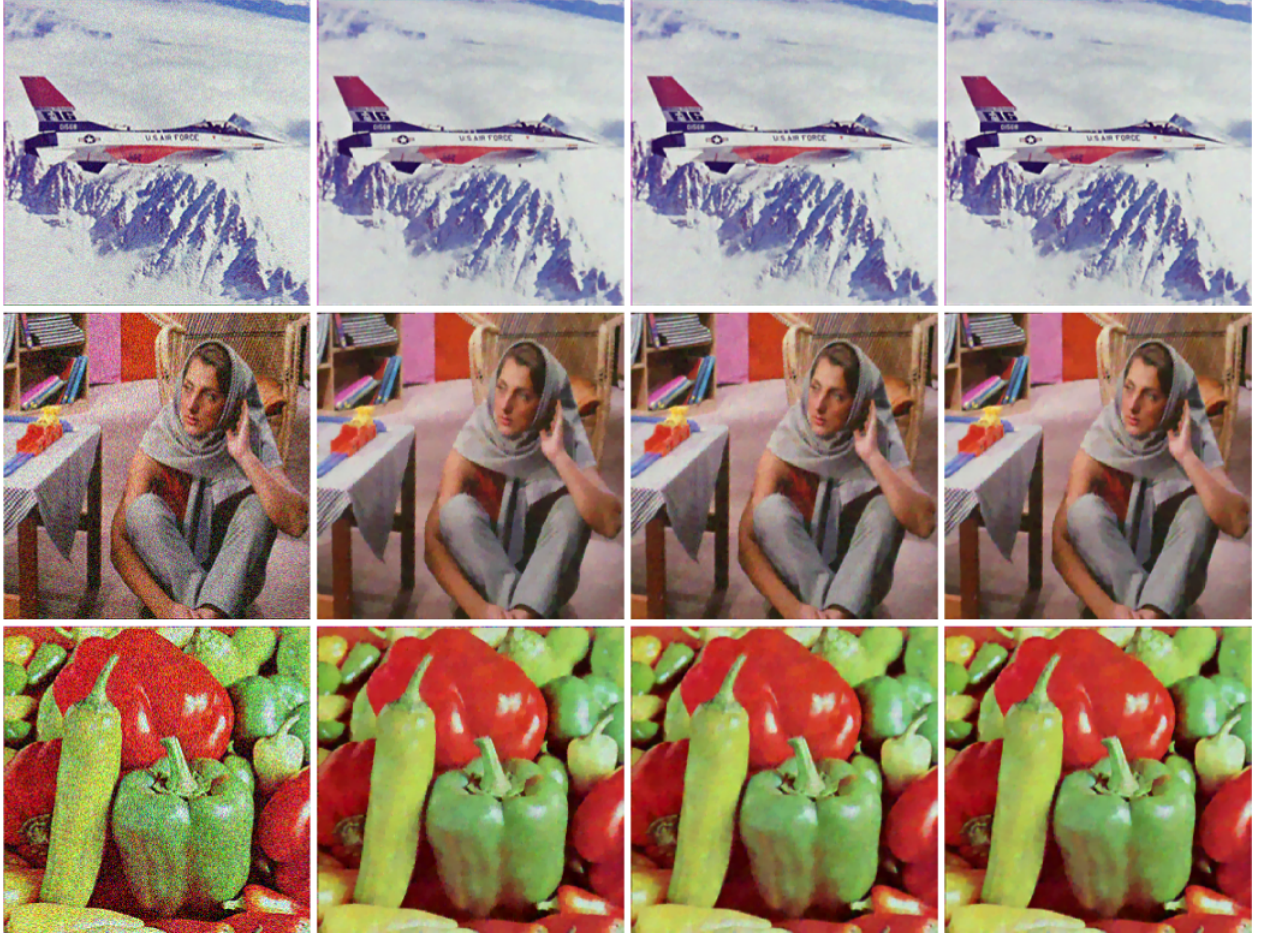


Fig 4 Compare the denoising effects of three models under various noise levels. The Gaussian noise levels from top to bottom are $\sigma = \{0.05, 0.1, 0.15\}$. The restoration results using VTV, STV, and WSTV are shown from the second column on the left to the last column on the right. The first column is the initial noise image.

279 5 Conclusion

280 In this paper, we propose an image denoising model based on weighted structure tensor total varia-
 281 tion. The core idea is that we use the anisotropic weighted matrix to the STV model to characterize
 282 local features of the images, which can effectively capture information about the restored images.
 283 In order to solve the corresponding WSTV model, we implement a fast first-order gradient projec-
 284 tion algorithm for the dual optimization problem. The experimental results demonstrate that our
 285 method has significant improvements compared to the TV-based and STV methods.

286 Although the WSTV model performs well, it takes a relatively long time when compared with

287 other methods. Therefore, it is meaningful for us to study the projection operators in the iteration
288 process. Customizing efficient algorithms according to a specific constraint set \mathcal{C} and the parameter
289 q in the unit norm ball $B_{\mathcal{S}_q}$ will help WSTV reduce the running time.

290 **Acknowledgments**

291 This research is supported by the National Natural Science Foundation of China (Grant No. 62073087).

292 **References**

- 293 1 R. Gonzalez, Digital image processing, *Pearson education india* (2009).
- 294 2 Z.-F. Pang et al., “Image restoration via the adaptive tvp regularization,” *Computers and*
295 Mathematics with Applications. **80**(5), 569-587 (2020).
- 296 3 C. Tian et al., “Deep learning on image denoising: An overview,” *Computers and Mathemat-*
297 ics with Applications. **131**, 251-275 (2020).
- 298 4 M. Elad, B. Kawar, and G. Vaksman, “Image Denoising: The Deep Learning Revolution and
299 Beyond-A Survey Paper,” *SIAM Journal on Imaging Sciences.* **16**(3), 1594-1654 (2023).
- 300 5 A. Danielyan, V. Katkovnik, and K. Egiazarian, “BM3D Frames and Variational Image
301 Deblurring,” *IEEE Transactions on Image Processing.* **21**(4), 1715-1728 (2012).
- 302 6 J. Koh, J. Lee, and S. Yoon, “Single-image deblurring with neural networks: A comparative
303 survey,” *Computer Vision and Image Understanding.* **203**, 103134 (2022).
- 304 7 B. Ivanov et al., “Accelerated Dai-Liao projection method for solving systems of monotone
305 nonlinear equations with application to image deblurring,” *Journal of Global Optimization.*
306 **85**(2), 377-420 (2023).

- 307 8 J.-F. Wu et al., "Low Dose CT Image Reconstruction Based on Structure Tensor Total Vari-
308 ation Using Accelerated Fast Iterative Shrinkage Thresholding Algorithm," *Sensors*. **20**(6),
309 1647 (2020).
- 310 9 M. Tsuneki et al., "Deep learning models in medical image analysis," *Journal of Oral Bio-*
311 *sciences*. **64**(3), 312-320 (2022).
- 312 10 B.-Z. Chen et al., "TransAttUnet: Multi-Level Attention-Guided U-Net With Transformer
313 for Medical Image Segmentation," *IEEE Transactions on Emerging Topics in Computational
314 Intelligence*. 1-14 (2023).
- 315 11 C.-Z. Wang et al., "A novel fuzzy hierarchical fusion attention convolution neural network for
316 medical image super-resolution reconstruction," *Information Sciences*. **622**, 424-436 (2023).
- 317 12 Y. Sui et al., "Scan-Specific Generative Neural Network for MRI Super-Resolution Recon-
318 struction," *IEEE Transactions on Medical Imaging*. **41**(6), 1383-1399 (2022).
- 319 13 L. Ma et al., "Unsupervised super-resolution reconstruction of hyperspectral histology im-
320 ages for whole-slide imaging," *Journal of biomedical optics*. **27**(5), 056502 (2022).
- 321 14 L. Rudin, S. Osher, and E. Fatemi, "Nonlinear total variation based noise removal algo-
322 rithms," *Physica D: Nonlinear Phenomena*. **60**(1-4), 259-268 (1992).
- 323 15 C. Vogel, Computational methods for inverse problems, *SIAM* (2002).
- 324 16 D. Strong and T. Chan, "Edge-preserving and scale-dependent properties of total variation
325 regularization," *IEEE Inverse problems*. **19**(6), S165 (2003).
- 326 17 M. Lysaker, A. Lundervold, and X.-C. Tai, "Noise removal using fourth-order partial differ-
327 ential equation with applications to medical magnetic resonance images in space and time,"
328 *IEEE Transactions on Image Processing*. **12**(12), 1579-1590 (2003).

- 329 18 I. Chan, A. Marquina, and P. Mulet, “High-order total variation-based image restoration,”
- 330 *SIAM Journal on Scientific Computing.* **22**(2), 503-516 (2000).
- 331 19 K. Bredies, K. Kunisch, and T. Pock, “Total generalized variation,” *SIAM Journal on Imaging*
- 332 *Sciences.* **3**(3), 492-526 (2010).
- 333 20 F. Knoll et al., “Second order total generalized variation (tgv) for mri,” *Magnetic Resonance*
- 334 *in Medicine.* **65**(2), 480-491 (2011).
- 335 21 G. Gilboa and S. Osher, “Nonlocal operators with applications to image processing,” *Multi-*
- 336 *scale Modeling and Simulation.* **7**(3), 1005-1028 (2009).
- 337 22 S. Lefkimiatis et al., “Structure tensor total variation,” *SIAM Journal on Imaging Sciences.*
- 338 **8**(2), 1090-1122 (2015).
- 339 23 E. Demircan-Tureyen and M. E. Kamasak, “On the Direction Guidance in Structure Tensor
- 340 Total Variation Based Denoising,” *Iberian Conference on Pattern Recognition and Image*
- 341 *Analysis.* 89-100 (2019).
- 342 24 I. Bayram and M. E. Kamasak, “Directional total variation,” *IEEE Signal Processing Letters.*
- 343 **19**(12), 781-784 (2012).
- 344 25 Z.-F. Pang et al., “Image denoising via a new anisotropic total-variation-based model,” *Signal*
- 345 *Processing: Image Communication.* **74**, 140-152 (2019).
- 346 26 A. Chambolle, “An algorithm for total variation minimization and applications,” *Journal of*
- 347 *Mathematical imaging and vision.* **20**, 89-97 (2004).
- 348 27 S. Lefkimiatis, J. P. Ward, and M. Unser, “Hessian schatten-norm regularization for linear
- 349 inverse problems,” *IEEE Transactions on Image Processing.* **22**(5), 1873-1888 (2013).

- 350 28 S. Lefkimiatis and S. Osher, “Nonlocal structure tensor functionals for image regulariza-
351 tion,” *IEEE Transactions on Computational Imaging*. **1**(1), 16-29 (2015).
- 352 29 A. Beck and M. Teboulle, “Fast gradient-based algorithms for constrained total variation
353 image denoising and deblurring problems,” *IEEE Transactions on Image Processing*. **18**(11),
354 2419-2434 (2009).
- 355 30 A. Beck and M. Teboulle, “A fast iterative shrinkage-thresholding algorithm for linear inverse
356 problems,” *SIAM Journal on Imaging Sciences*. **2**(1), 183-202 (2009).
- 357 31 S. Suvrit, “Fast projections onto $\ell_{1,q}$ -norm balls for grouped feature selection,” *Machine
358 Learning and Knowledge Discovery in Databases, Springer, Berlin.* Vol. **3**, 305–317 (2011).
- 359 32 X. Bresson and T. F. Chan, “Fast dual minimization of the vectorial total variation norm
360 and applications to color image processing,” *Inverse problems and imaging*. **2**(4), 455-484
361 (2008).

362 **Xiuhan Sheng** received his BS degree in science from Henan Agricultural University in 2021.
363 Currently, he is pursuing a master’s degree at the School of Mathematics and Statistics, Guangdong
364 University of Technology, Guangzhou, China. His research interest is mainly in image restoration.

365 **Lijuan Yang** received her BS degree in management from Hainan Medical University in 2021.
366 Currently, she is pursuing a master’s degree at the School of Mathematics and Statistics, Guang-
367 dong University of Technology, Guangzhou, China. Her research interest is mainly in machine
368 learning.

369 **Jingya Chang** received her BS degree in science from Henan Normal University, her MS degree
370 in science from Nanjing Normal University, and her PhD in applied mathematics from Hong Kong

³⁷¹ Polytechnic University in 2006, 2009, and 2018, respectively. Her research interests include non-
³⁷² linear optimization, tensor optimization, and their applications in image processing and machine
³⁷³ learning.

³⁷⁴ **List of Figures**

- ³⁷⁵ 1 Twelve 256×256 test images. From left to right and top to bottom: Camera-
³⁷⁶ man, House, Peppers, Starfish, Butterfly, Parrot, Baboon, Boats, Colored butterfly,
³⁷⁷ Babara, Colored peppers and Airplane.
- ³⁷⁸ 2 Compare the denoising effects of various models on grayscale images at the Gaus-
³⁷⁹ sian noise level $\sigma = 0.05$. From left to right are the image restoration results
³⁸⁰ obtained using TV, ATV, STV, and the proposed model (WSTV). The first row of
³⁸¹ each image represents the complete restored image. The second row of each image
³⁸² is a part of the restored image.
- ³⁸³ 3 Compare the denoising effects of various models on grayscale images at the Gaus-
³⁸⁴ sian noise level $\sigma = 0.1$. From left to right are the image restoration results ob-
³⁸⁵ tained using TV, ATV, STV, and the proposed model (WSTV). The first row of
³⁸⁶ each image represents the complete restored image. The second row of each image
³⁸⁷ is the difference between the restored image and the original image. The colorbar
³⁸⁸ displays more efficient restorations if the color is more shaded.
- ³⁸⁹ 4 Compare the denoising effects of three models under various noise levels. The
³⁹⁰ Gaussian noise levels from top to bottom are $\sigma = \{0.05, 0.1, 0.15\}$. The restoration
³⁹¹ results using VTV, STV, and WSTV are shown from the second column on the left
³⁹² to the last column on the right. The first column is the initial noise image.

393 **List of Tables**

394 1 Compare the PSNR and SSIM of different models in grayscale image denoising.

395 2 Compare the PSNR and SSIM of different models in color image denoising.